Effective dielectric function of porous $Pb(Mg_{1/3}Nb_{2/3})O_3$ ceramics

D. Nuzhnyy,[1] J. Petzelt,[1] I. Rychetsky,[1] and G. Trefalt[2,3,*]
[1]*Institute of Physics AS CR, 18221 Prague 8, Czech Republic*
[2]*Jozef Stefan Institute, SI-1000 Ljubljana, Slovenia*
[3]*Center of Excellence NAMASTE, Jamova cesta 39, 1000 Ljubljana, Slovenia*
(Received 16 January 2014; revised manuscript received 27 May 2014; published 16 June 2014)

A set of $Pb(Mg_{1/3}Nb_{2/3})O_3$ (PMN) relaxor ceramics with different porosities (66–96% of theoretical density) was processed from the pure perovskite PMN powder by varying the sintering temperature (930–980 K) and isostatic pressure. The effective room temperature permittivity at 100 Hz varied correspondingly from ∼4000 to ∼15 000. We measured and fitted the room temperature infrared (IR) reflectivity of corresponding polished ceramics, from which the effective dielectric function was obtained. The results were compared with the low-frequency permittivity data and discussed using several effective medium models. The best results were obtained using the Lichtenecker model (with the exponent $\alpha \approx 0.2$), which fits quite well the IR spectra as well as the static permittivity for all the porosity values. Also the simulation using the finite element method supported the same model. It allows us to conclude that the samples show quite complex shape and topology of the pores, but all of the pores show similarity with a weak nonzero percolation (open porosity).

DOI: 10.1103/PhysRevB.89.214307 PACS number(s): 63.20.−e, 77.22.−d, 78.30.−j, 02.70.Dh

I. INTRODUCTION

$Pb(Mg_{1/3}Nb_{2/3})O_3$ (PMN) is the best studied classical relaxor ferroelectric [1]. Its dielectric response in a broad frequency range up to the infrared (IR) was reported several times [1–5], including responses of ceramics [6] and thin films [7,8]. In the case of ceramics, the grain-size effect on the dielectric response is also quite remarkable, similar to other high permittivity materials, as reviewed in Ref. [9]. For PMN it appears that the grain boundaries partly block the flipping of polar nanoregions close to grain boundaries, which reduces the effective permittivity with the grain-size reduction. However, for μm-sized and larger grains, the dielectric size effect can be neglected. Porosity is also naturally expected to reduce the dielectric response in high-permittivity materials, but, to our knowledge, this effect was not yet been systematically investigated. Recently, a purely perovskite PMN powder has been processed, eliminating the problem with secondary pyrochlore phase, which allowed us to prepare high quality ceramics [10]. Here we report on processing of similar ceramics with varying porosity and studied their effective dielectric response at low frequencies as well as their IR response from IR reflectivity, modelling it using the effective medium approach (EMA) and finite element method.

II. EXPERIMENTAL

The PMN ceramics were synthesized by controlled agglomeration of particles in an aqueous suspension. This method is described in detail in Refs. [10] and [11]; here we only briefly present the summary of the synthesis and the data relevant for this work.

Aqueous suspensions of mixture of PbO (99.9%), Nb_2O_5 (99.9%), and $(MgCO_3)\cdot 4Mg(OH)_2\cdot 4H_2O$ (41.91% of MgO) were prepared in the molar ratio corresponding to stoichiometry of PMN. Ammonia solution (25 wt.%) was added to adjust the pH of the suspension to 12.5. The suspension was milled in an attrition mill for 3 h at 800 rpm using 3-mm yttria-stabilized zirconia balls. After drying at 100 °C, the powder mixture was heated at 900 °C for 5 h. The calcined PMN powder was then isostatically pressed into compacts at two different isostatic pressures, namely 100 MPa and 300 MPa. In order to vary the final density of the ceramics, the compacts were sintered at different temperatures from 930–980 °C for 2 h. The densities were determined from the dimensions and mass of the pellets, and they are expressed as the percentage of the theoretical density, which is equal to 8.13 g/cm^3.

The polished ceramic samples were examined using the field-emission scanning electron microscope JSM-7600F (FE-SEM) (JEOL Ltd., Tokyo, Japan) (see Fig. 1). The capacitance and dielectric losses at room temperature were measured with HP 4192A LCR meter (Yokogawa Hewlett-Packard) in the frequency range of 100 Hz–100 kHz.

The IR reflectivity spectra in the 20–700 cm^{-1} range were measured under near-normal incidence at room temperature on polished ∼1-mm-thick (opaque) samples using Fourier transform IR spectrometer Bruker IFS 113v equipped with pyroelectric deuterated triglycine sulfate detector. In the THz range, the dielectric response of the 95.7% dense sample polished down to ∼43 μm was obtained using the time-domain THz transmission spectrometer based on a Ti:sapphire femtosecond laser [12]. For generation of the THz pulses, an interdigitated photoconducting GaAs switch was used. To detect the transmitted THz pulses, a plate of the [110] ZnTe crystal was used for electro-optic sampling.

III. RESULTS

In Fig. 2, we present room temperature IR reflectivities of our samples with porosity up to 23.7%. The surface of the sample with the highest porosity of 33.9%, which is omitted in Fig. 2, could not be properly polished, so its IR reflectivity was affected by scattering. The reflectivity of the densest sample

*Current address: Department of Inorganic and Analytical Chemistry, University of Geneva, Sciences II, 30, Quai Ernest-Ansermet, CH-1211 Geneva.

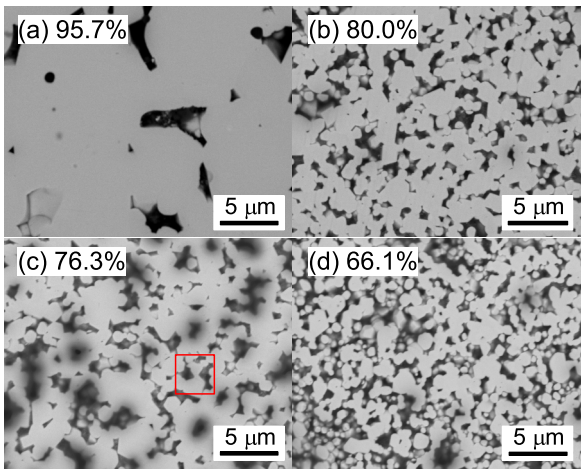

FIG. 1. (Color online) SEM pictures of the polished PMN ceramics with (a) 95.7%, (b) 80.0%, (c) 76.3%, and (d) 66.1% of theoretical density. The region used for finite element modelling is shown by the red frame in (c).

was normalized to the THz reflectivity calculated from the THz transmission, which is known to be of higher accuracy, and all the other reflectivity spectra were normalized by the same coefficient (~0.91). The reflectivity spectra were fitted using the standard factorized form of the dielectric function [13]. To also include the low frequency permittivity into the fit, a product form of Debye relaxation [14] (of relaxation frequency ω_{TR} fixed at ~1 GHz, as estimated from the earlier experiments [3,8] and fitted dielectric strength by changing ω_{LR}) was added to obtain the overall dielectric response:

$$\varepsilon(\omega) = \varepsilon_\infty \frac{\omega_{LR} + i\omega}{\omega_{TR} + i\omega} \prod_j \frac{\omega_{LOj}^2 - \omega^2 + i\omega\gamma_{LOj}}{\omega_{TOj}^2 - \omega^2 + i\omega\gamma_{TOj}},$$
$$R(\omega) = \left| \frac{\sqrt{\varepsilon(\omega)} - 1}{\sqrt{\varepsilon(\omega)} + 1} \right|^2, \quad (1)$$

where ω_{TOj} and ω_{LOj} denote the transverse and longitudinal frequency of the jth polar phonon, respectively, and γ_{TOj} and γ_{LOj} denote their corresponding damping constants. The high-frequency permittivity ε_∞ results from the electron absorption processes in the ultraviolet range. The fitted reflectivity spectra are also shown in Fig. 2, as well as the corresponding calculated complex dielectric functions in the IR-THz range using Eq. (1).

IV. EMA MODELLING

To describe the effect of porosity on the effective dielectric response, first we tried to apply the well-known Bruggeman

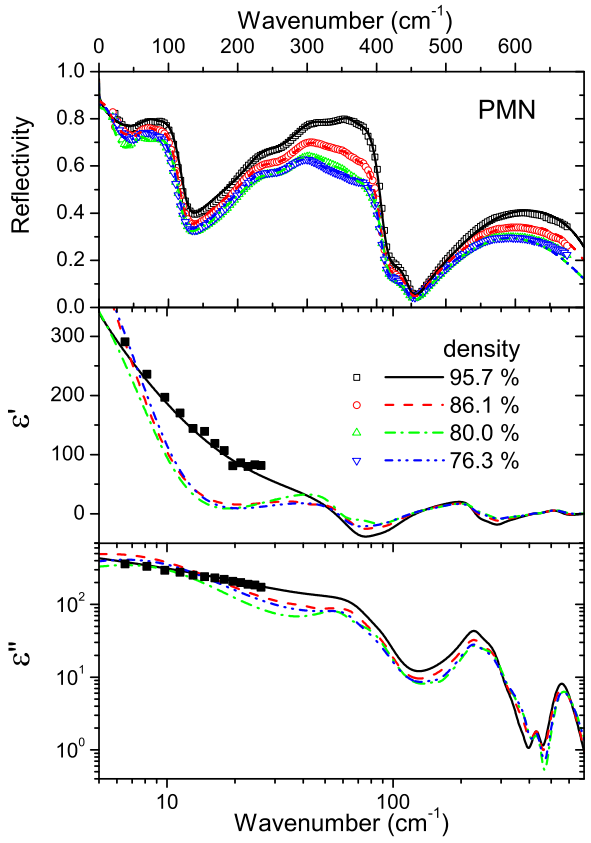

FIG. 2. (Color online) Room temperature IR reflectivities (empty symbols) and their fits using Eq. (1) (lines) and complex dielectric functions calculated from parameters of the fits (lines) along with the THz data for the 95.7% sample (full symbols). The reflectivity of the 66.1% dense sample is omitted since its surface quality was appreciably deteriorated by scattering.

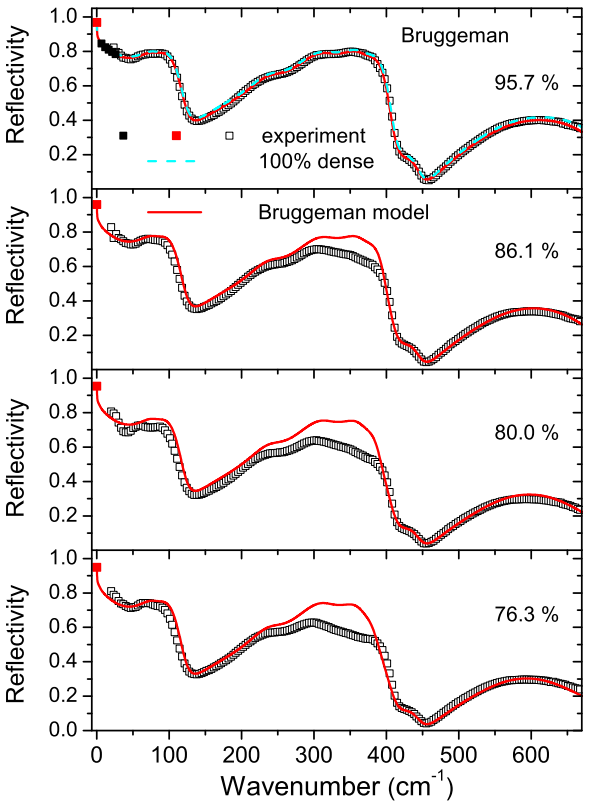

FIG. 3. (Color online) Room temperature IR reflectivities (empty symbols), reflectivity calculated from the THz response and at 100 Hz (full symbols), and their modelling with the Bruggeman formula (2) (solid lines). The reference spectrum of the fully dense PMN ceramics is shown by the dashed line.

model [15],

$$(1-x)\frac{\varepsilon_1-\varepsilon_{\text{eff}}}{\varepsilon_1+2\varepsilon_{\text{eff}}}+x\frac{\varepsilon_2-\varepsilon_{\text{eff}}}{\varepsilon_2+2\varepsilon_{\text{eff}}}=0. \quad (2)$$

The dielectric response ε_1 of the neat (fully dense) PMN was first calculated from the fitted dielectric function of the 95.7% dense ceramics taking into account its porosity of 4.3% with $\varepsilon_2 = 1$. Then ε_{eff} was calculated as the effective dielectric response, and the corresponding effective IR reflectivities were calculated for all the samples. The modelled reflectivities are shown in Fig. 3.

Since the modelled IR reflectivity spectra and particularly the low-frequency permittivities were not in a good agreement with the experimental data, as the second step we used the Lichtenecker model [16],

$$\varepsilon_{\text{eff}}^{\alpha}=(1-x)\varepsilon_1^{\alpha}+x\varepsilon_2^{\alpha}, \quad -1\leqslant\alpha\leqslant 1. \quad (3)$$

For α near to zero, this empirical formula is known to correspond to rather complex topologies within EMA modelling [17]. For the positive α, both components are partially percolated for all compositions x, and for the negative α, neither of the components is percolated, again independently of x. The limiting case of $\alpha = 0$ corresponds to frequently used logarithmic mixing formula (the so-called geometrical mean model). Like in the previous fitting procedure, the dielectric response ε_1 of the neat PMN component was calculated from the fit of IR reflectivity of the PMN ceramics with the highest density (95.7%), and after that this dielectric function was used to calculate the effective properties of the other ceramics. Now α was modified as a fitting parameter, and the best results were achieved with $\alpha = 0.2$. The modelled IR reflectivity is shown in Fig. 4. For the densest sample, the dielectric response from the Lichtenecker model replicates the directly fitted dielectric function using Eq. (1), and for the other samples

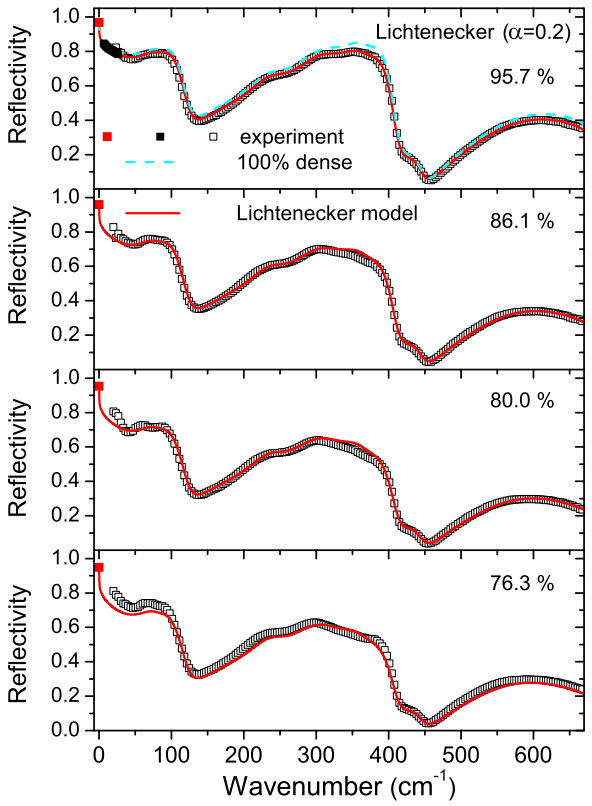

FIG. 4. (Color online) Room temperature IR reflectivities (empty symbols), reflectivity calculated from the THz response and at 100 Hz (full symbols), and their modelling with the Lichtenecker formula (3) (lines). The reference spectrum of the fully dense PMN ceramics is shown by the dashed line.

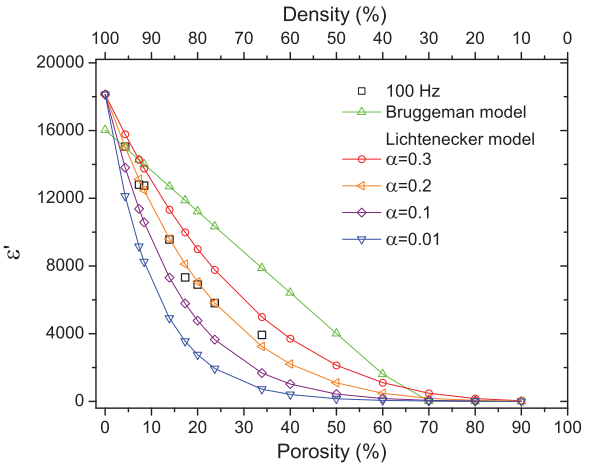

FIG. 5. (Color online) Porosity dependence of the effective static permittivity calculated from the Bruggeman and Lichtenecker model (for several α values) compared with the experimental data at 100 Hz. Calculated static permittivity of dense PMN component for modelling is shown by the symbols at zero porosity.

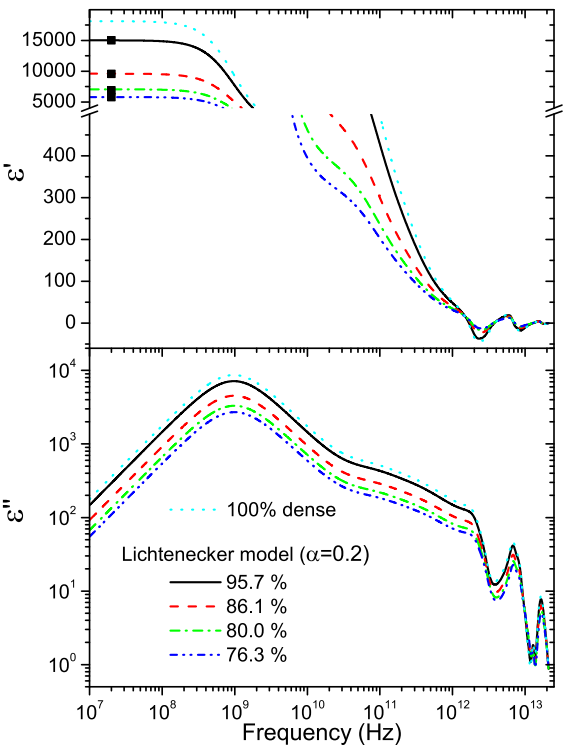

FIG. 6. (Color online) Dielectric functions of PMN in a broad frequency range calculated using the Lichtenecker model (solid lines) and the dielectric permittivity measured at 100 Hz (full symbols).

the differences are rather small. We note that the reference reflectivity spectrum of the fully dense PMN (dashed line in Fig. 4) differs slightly from that in Fig. 3, obtained from the Bruggeman model, but the modelled spectra of the densest sample are identical for both models.

The α value has particularly strong influence on the effective permittivity data, as documented in Fig. 5, where several mixing formulae (including the Bruggeman model) are compared with the experimental permittivity values at 100 Hz. The Lichtenecker model with the same $\alpha = 0.2$ as the fit of IR reflectivities gives by far the best result. For this model we have plotted the calculated effective complex dielectric functions from 10^7 Hz up to the IR phonon range in Fig. 6. These broad-band dielectric responses fit well the low-frequency dielectric permittivity, as well as the IR reflectivities, and within the Lichtenecker model the relaxation frequency at 1 GHz is not apparently influenced by the porosity.

V. FINITE ELEMENT MODELLING

Using the FE-SEM pictures in Fig. 1, it is tempting to calculate the dielectric spectra using the finite element approach and compare them with the experimental data. In order to perform a 3-dim. model of the PMN-pore composite, which would yield a cross section similar to pictures in Fig. 1, the following simple model was constructed. The cubic symmetry of PMN and traces of grain facets observed in Fig. 1 make reasonable assumption of the cubic grains, however, the grain shape is expected to play a minor role in the disordered sample. The PMN grains were assumed of cubic shape with rounded edges, as created by the equation $(x - x_0)^6 + (y - y_0)^6 + (z - z_0)^6 = r^6$, where (x_0, y_0, z_0) is the grain center. Inside the box of $512 \times 512 \times 512$ voxels, N grains with random positions and orientations were generated. For simplicity, all grains had the same size r. Parameters of the model are chosen such that two grains can overlap, i.e., random distance between their centers Δ can be smaller than $2r$, but at the same time the grains cannot come too close, i.e., Δ is always larger than $N\delta$. Parameters we have considered are $N = 100$, $r = 57$, and $\delta = 0.2$, and then the calculated grain volume fraction of the randomly generated structure is always near 0.758 (porosity 0.252). An example of the generated three-dimensional (3D) structure and typical cross section are shown in Fig. 7. The model describes a small region of the real ceramic sample denoted by the red frame in Fig. 1(c). Due to the finite box size, fluctuations in the calculated quantities are expected. Therefore 10 sets of randomly distributed grains were generated in order to smooth out the fluctuations. The segmented 3D images were meshed using CGAL library [18], and Maxwell equations were solved using the finite element method (FreeFem++) [19]. The effective permittivity $\varepsilon_{\rm eff}(\varepsilon_1,\varepsilon_2)$, which depends on permittivities of grains and pores, is obtained from the relation $\langle D\rangle = \varepsilon_0\varepsilon_{\rm eff}\langle E\rangle$, where $\langle\ldots\rangle$ is the volume average. Instead of calculating the effective permittivity for a broad range of frequencies, it is more convenient to work with material-independent structural quantities, namely the percolation strengths V_1, V_2, and the spectral function $v_{12}(n)$, which occur in the Bergman representation of the effective permittivity [20]

$$\varepsilon_{\rm eff} = V_1\varepsilon_1 + V_2\varepsilon_2 + \int_0^1 v_{12}(n)\frac{\varepsilon_1\varepsilon_2}{(1-n)\varepsilon_2 + n\varepsilon_1}dn, \quad (4)$$

where the first two terms describe percolated clusters of grains and pores, respectively, and the last term describes the contribution of nonpercolated clusters, which are influenced by the depolarizing field in various manners. The spectral function can be obtained using the inverse formula [20]

$$(1-n)v_{12}(n) = \lim_{\delta\to 0}\pi^{-1}Im\left[\varepsilon_2^{-1}\varepsilon_{\rm eff}\left(1 - \frac{1}{n+i\delta}, 1\right)\right], \quad (5)$$

where the depolarization factor n is running from 0 to 1 and $\varepsilon_{\rm eff}$ is taken with arguments $\varepsilon_1 = 1 - \frac{1}{n+i\delta}$ and $\varepsilon_2 = 1$. The spectral function $v_{12}(n)$ characterizes statistical appearance of grains or grain clusters in the composite with the depolarization factor n.

The spectral functions for 10 sets of grains together with the spectral function of the Lichtenecker formula are plotted in Fig. 8. The higher decay of data occurs only near $n \approx 0$ and 1. Good agreement with the Lichtenecker formula is observed for the small exponent $\alpha \sim 0.1$–0.3, discrepancy occurs only near $n \approx 0$ and 1. Note that the Lichtenecker model as well as our simulation yield quite equally distributed $v_{12}(n)$, as expected for a disordered composite. Numerical calculation gives the average percolation strength $V_1 \sim 0.537$, and the

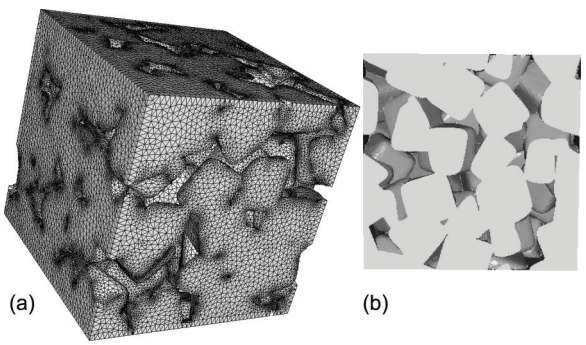

FIG. 7. (a) The generated 3D structure of the region shown in Fig. 1(c) and (b) typical cross section of 3D structure.

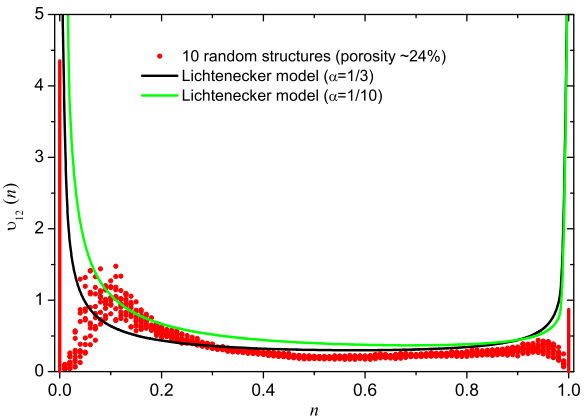

FIG. 8. (Color online) Finite element calculated spectral functions $v_{12}(n)$ for 10 random structures of grains (symbols) compared with the spectral functions of the Lichtenecker formula (3) (solid lines).

spectral function approaches 0 for small n. On the other hand, the Lichtenecker formula with $\alpha = 0.1$ diverges at small n, but $V_1 = x^{10} \sim 0$ is very small. This discrepancy could be explained by the finite size of our model, in which the maximal size of the nonpercolated clusters cannot exceed the size of the box; therefore, larger clusters contribute to the percolation strength and not to the spectral function at small n. Similar behavior is observed also near $n \sim 1$. In Fig. 8 the calculated percolation strengths are represented by thick vertical lines at 0 and 1.

VI. DISCUSSION AND CONCLUSIONS

The IR reflectivity of the densest PMN ceramics is in a good agreement with previously published data on single crystals [4,5] as well as dense coarse-grain ceramics [6,8]. As expected, the increasing porosity reduces slightly the overall IR reflectivity, which is revealed in slightly reduced mode strengths and increased damping parameters. Fit using the Lichtenecker model with $\alpha = 0.2$ is quite good (see Fig. 4), and the highest confidence in its relevance is given by modelling of the low-frequency permittivity, which is even more sensitive to the α value (Fig. 5), the best fit yielding the same $\alpha = 0.2$. The second striking feature is the independence of the best model of the degree of porosity. It indicates that the different sintering conditions yield the same topology and shape of pores in the ceramics. But the topology is quite complex with a rather homogeneous distribution of depolarization factors n and nonzero percolation of pores even in the densest ceramics (open porosity). This is confirmed also by modelling using the finite element method. It shows that the spectral function gives a smooth function of n very similar to that of the Lichtenecker model. Both types of models yield nonzero percolation values for both components, indicated by the divergences of the spectral function at $n = 0$ and 1.

ACKNOWLEDGMENTS

This research was supported by the Czech Science Foundation Project No. P204/12/0232. G.T. would like to acknowledge the financial support of Slovenian Research Agency under Grant No. P2-0105. The authors would like also to thank Ms. Brigita Kmet for the help with FE-SEM imaging.

[1] R. A. Cowley, S. N. Gvasaliya, S. G. Lushnikov, B. Roessli, and G. M. Rotaru, Adv. Phys. **60**, 229 (2011).
[2] V. Bovtun, J. Petzelt, V. Porokhonskyy, S. Kamba, and Y. Yakimenko, J. Eur. Ceram. Soc. **21**, 1307 (2001).
[3] V. Bovtun, S. Kamba, A. Pashkin, M. Savinov, P. Samoukhina, J. Petzelt, I. P. Bykov, and M. D. Glinchuk, Ferroelectrics **298**, 23 (2004).
[4] S. A. Prosandeev, E. Cockayne, B. P. Burton, S. Kamba, J. Petzelt, Y. Yuzyuk, R. S. Katiyar, and S. B. Vakhrushev, Phys. Rev. B **70**, 134110 (2004).
[5] J. Hlinka, T. Ostapchuk, D. Noujni, S. Kamba, and J. Petzelt, Phys. Rev. Lett. **96**, 027601 (2006).
[6] V. Bovtun, S. Veljko, M. Savinov, A. Pashkin, S. Kamba, and J. Petzelt, Int. Ferroelectrics **69**, 3 (2005).
[7] S. Kamba, M. Kempa, V. Bovtun, J. Petzelt, K. Brinkman, and N. Setter, J. Phys.: Condens. Matter **17**, 3965 (2005).
[8] V. Bovtun, S. Veljko, S. Kamba, J. Petzelt, S. Vakhrushev, Y. Yakymenko, K. Brinkman, and N. Setter, J. Eur. Ceram. Soc. **26**, 2867 (2006).
[9] J. Petzelt, Ferroelectrics **400**, 117 (2010).
[10] G. Trefalt, B. Malič, D. Kuščer, J. Holc, and M. Kosec, J. Am. Ceram. Soc. **94**, 2846 (2011).
[11] G. Trefalt, B. Malič, J. Holc, H. Uršič, and M. Kosec, J. Am. Ceram. Soc. **95**, 1858 (2012).
[12] P. Kužel, H. Němec, F. Kadlec, and C. Kadlec, Opt. Express **18**, 15338 (2010).
[13] F. Gervais, in *Infrared and Millimeter Waves*, edited by K. J. Button (Academic, New York, 1983), Vol. 8, p. 279.
[14] J. L. Ribeiro, L. G. Vieira, M. R. Chaves, A. Almeida, S. Sarmento, and A. Klöpperpieper, J. Phys.: Condens. Matter **16**, 2733 (2004).
[15] D. A. G. Bruggeman, Ann. Phys. **416**, 636 (1935).
[16] K. Lichtenecker, Phys. Z. **27**, 115 (1926).
[17] T. Zakri, J. P. Laurent, and M. Vauclin, J. Phys. D: Appl. Phys. **31**, 1589 (1998).
[18] CGAL, Computational Geometry Algorithms Library, http://www.cgal.org
[19] F. Hecht, J. Numer. Math. **20**, 251 (2012).
[20] I. Rychetsky and A. Klic, Ferroelectrics **427**, 143 (2012).